Aero-optical and fluidic studies of a forced subsonic compressible shear layer

Carson M. Kipp[a], Jacob Caldwell[a], R. Mark Rennie[a], and Stanislav Gordeyev[a]

[a]Institute of Flow Physics and Control, Aerospace and Mechanical Engineering Department, University of Notre Dame, Notre Dame, IN, USA

ABSTRACT

Predicting aero-optical distortions induced by subsonic compressible shear layers is essential for developing effective feed-forward adaptive optic compensation systems for directed energy platforms using common beam director geometries. While the established "Weakly Compressible Model" (WCM) presented in Ref. 1 reasonably predicts path-integrated wavefront aberrations, recent computational fluid dynamics (CFD) simulations reveal that it fails to capture the sharp, localized stagnation temperature and density gradients that form along the slip lines of vortical structures. This study presents a continuation of the experimental investigation in Ref. 2 to validate the thermo-fluid mechanisms proposed in Ref. 3. Experiments were conducted in a compressible shear layer wind tunnel at a convective Mach number of $M_c \approx 0.23$, regularized via acoustic voice-coil excitation at a fundamental frequency of 750 Hz. The fluctuating pressure and temperature fields were mapped using an array of wall-normal unsteady pressure transducers paired with a custom frequency-compensated cold-wire anemometer ($\tau_w \approx 1.8$ ms). To characterize the optical effects of the flow environment, spanwise and cross-stream digital holographic wavefront sensing (DHWFS) was coupled with narrow depth-of-field self-aligned focusing schlieren (SAFS) imaging to examine the shear layer on a two-dimensional and path-integrated basis. Phase-averaged cross-stream DHWFS results reveal that spanwise non-uniformities are non-negligible, providing experimental evidence that path-integrated effects may smooth out the intense, small-scale localized thermodynamic gradients when viewed in the spanwise direction, offering an explanation for why lower-fidelity two-dimensional models can inadvertently mimic path-integrated optical data.

Keywords: Aero-optics, digital holography, self-aligned focusing Schlieren, cold-wire anemometry, thermodynamic gradients

1. INTRODUCTION

Aero-optics is the study of optical effects induced by compressible flows. These effects arise from the relationship between fluid density, ρ, and the index of refraction, n, as defined by the Gladstone-Dale equation:

$$n = 1 + \mathrm{K_{GD}}\rho, \tag{1}$$

where $\mathrm{K_{GD}}$ denotes the Gladstone-Dale coefficient ($\mathrm{K_{GD}} \approx 2.223 \times 10^{-4}\,\mathrm{m^3/kg}$).[4]

One active area of research within the aero-optics community is the subsonic compressible shear layer, which features highly variable density and refractive index fields. Compressible shear layers commonly form over standard beam-director geometries, such as hemispherical turrets, at the interface between the freestream flow and the separated wake region.[5] Accurately predicting the thermodynamic and density fields of the shear layer, along with the physical mechanisms that generate them, is therefore an important step in improving the performance of such systems.[5] For example, developing high-fidelity models of the optical effects of a subsonic compressible shear layer would enable improved feed-forward adaptive optic compensation.

Previous studies have attempted to model subsonic (or weakly compressible) shear layers under the assumption that compressibility does not strongly affect the development of the underlying velocity field, which is dominated by large-scale vortical structures. Instead, Fitzgerald and Jumper[1] posited that compressibility primarily manifests in the thermodynamic field. Building on this assumption, researchers simulated the velocity

*Corresponding Author. E-mail: ckipp@nd.edu, Telephone: (248) 766-2860

Unconventional Imaging, Sensing, and Adaptive Optics 2026, edited by Jean Dolne, Santasri Bose-Pillai, Matthew Kalensky, Proc. of SPIE Vol. 14229, 142290Z · 2026 Published by SPIE
0277-786X · doi: 10.1117/12.3113181

field using an incompressible discrete vortex method and subsequently recovered the associated pressure, temperature, and density distributions through a thermodynamic model called the "Weakly Compressible Model" (WCM). The WCM successfully predicted optical distortions and was therefore assumed to capture the relevant mechanisms of the shear layer's density field. A flowchart illustrating this computational process (adapted from Ref. 6) is shown in Fig. 1.

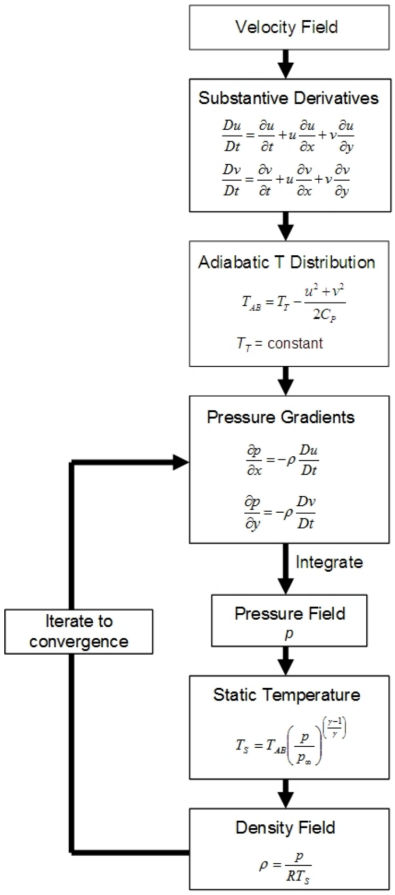

Figure 1: Weakly compressible model flow chart adapted from Ref. 6

The model first determines an adiabatic temperature distribution from a pre-determined velocity field. Using the prescribed velocity field and initial density estimate, the unsteady Euler equations are applied to compute the corresponding pressure gradients and then integrated to produce the pressure field. This pressure field and previously computed adiabatic temperature distribution are used to find the static temperature via isentropic relations, allowing the density field to be resolved through the ideal gas law. Finally, this updated density field is then fed back into the Euler equations to recompute the pressure gradients, repeating the cycle until the thermodynamic fields reach convergence.[1,6] However, subsequent studies revealed discrepancies in the magnitude of the predicted density gradients, particularly along the slip lines between vortical structures, when compared with computational fluid dynamics (CFD) simulations.[6,7] More recently, complementary two-dimensional CFD simulations and experimental studies provided strong evidence for the existence of sharp density gradients in weakly compressible shear layers.[3,8,9] Specifically, these CFD simulations identified the stagnation temperature field as the source of these gradients, whereas the WCM fails to predict such sharp stagnation temperature or density gradients.

Furthermore, Ref. 1 argued that because spatial changes in stagnation temperature are driven primarily by

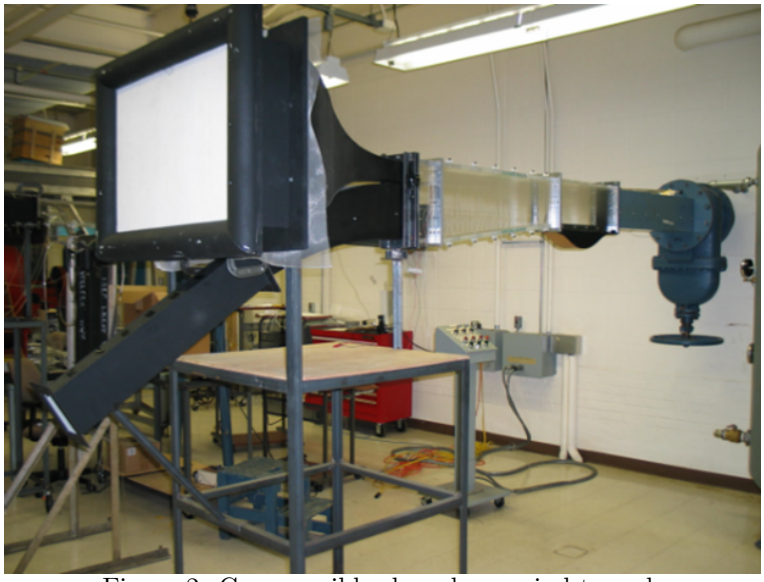

Figure 2: Compressible shear layer wind tunnel.

temporal pressure fluctuations,

$$\rho C_p \frac{DT_0}{Dt} = \frac{\partial P}{\partial t}, \tag{2}$$

and because the pressure field is smooth, sharp temperature gradients should not appear in shear layers. However, Refs. 9 and 3 demonstrated that fluid particles passing through the unsteady pressure wells associated with vortical structures undergo localized heating and cooling. In effect, the compressible work performed by the unsteady pressure field directly alters the energy of fluid particles, with the slip line between the high- and low-speed flows, which constitutes a streamline, acting as a thermal boundary between the heated and cooled fluid entrained by the large-scale structures, producing sharp thermodynamic gradients.

Although omitting this individual-particle thermodynamic history leads to artificially weak density gradients, the WCM still managed to correctly predict path-integrated optical distortions. Several factors have been proposed to explain this phenomenon, including insufficient wavefront sensing resolution.[10] However, one factor that remains unexamined is the effect of path-integrated wavefront sensing performed along a non-uniform optical path. The spatial integration across the spanwise direction would inherently smooth the perceived density gradients compared to their two-dimensional counterparts. It is therefore suspected that the WCM, which operates on a two-dimensional basis, inadvertently captures this three-dimensional line-of-sight smoothing effect while failing to accurately model the true underlying 2D thermodynamic processes.

The present study continues the work presented in Ref. 2 and aims to experimentally validate the thermo-fluid mechanisms proposed in Refs. 9 and 3, and investigate the influence of spanwise non-uniformities and path-integrated wavefront sensing on shear layer density gradient predictions. To validate the proposed mechanisms, the 2D thermal field of the shear layer is evaluated using a frequency-compensated cold-wire anemometer paired with simultaneous wall-normal static pressure measurements. To isolate the effects of path integration on perceived density gradients, spanwise and cross-stream digital holographic wavefront sensing measurements are coupled with self-aligned focusing schlieren imaging.

2. EXPERIMENTAL APPROACH

2.1 Compressible Shear Layer Wind Tunnel

The experimental studies were conducted in the Compressible Shear Layer Wind Tunnel (CSLWT) at the University of Notre Dame, shown in Fig. 2. A shear layer is formed by combining inlets of differing flow velocities at a splitter plate. The high- and low-speed inlets form freestream flows at $M_2 \approx 0.56$ ($U_2 \approx 186$ m/s) and

$M_1 \approx 0.08$ ($U_1 \approx 27$ m/s) respectively. The resulting weakly-compressible shear layer has a convective Mach number of $M_c \approx 0.23$, where the convective Mach number is defined as

$$M_{\text{conv}} = \frac{U_2 - U_1}{a_2 + a_1}, \tag{3}$$

where a represents the speed of sound and subscripts 1 and 2 denote the low- and high speed regions of the shear layer, respectively.[11] Constant stagnation temperature is ensured between inlets due to the indraft design which draws air from a common laboratory environment. In particular, the ambient stagnation temperature during flow diagnostic testing was recorded to be 295.2 K. In order to maintain constant static pressure within the test section, high pressure loss straw boxes are used to reduce the total pressure of the low speed flow, generating an inlet-matched static pressure of ≈ 80600 Pa.

At the trailing edge of the splitter plate, an array of voice coil actuators is used to provide flow excitation.[12] This forcing is designed to regularize the shear layer formation and vortex pairing mechanisms while improving spanwise uniformity by adding energy in resonance with the most unstable frequency and its subharmonic to the shear layer. Together, these effects increase the two-dimensionality of the flow and enable phase-locked measurements of static temperature, static pressure, and wavefront measurements by promoting the formation and deterministic interaction of coherent structures at the measurement location. The extent to which flow excitation improves spanwise uniformity and regularizes the flow in order to form a uniform optical path will be investigated in a later section. To apply the most effective excitation, the shear layer must be forced at the frequency of the most unstable mode, f_e, and its subharmonic, $f_{e/2}$,[13] regularizing the shear layer just upstream of the measurement location. To identify f_e and $f_{e/2}$, the power spectral density of the forced shear layer was tested across a range of candidate frequencies from 650 to 1200 Hz, revealing that the shear layer responded most strongly at $f_e = 750$ Hz. Consequently, the shear layer in this study was forced at this frequency along with its subharmonic (375 Hz) at 10% of the fundamental amplitude.[13]

A schematic of the experimental setup, showing the temperature, pressure, and spanwise wavefront measurement locations within the CSLWT test section, is shown in Fig. 3.

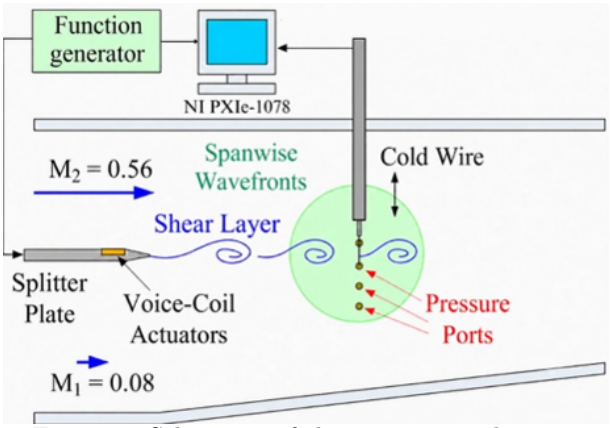

Figure 3: Schematic of the experimental setup.

2.2 Flow Diagnostics

The setup shown in Fig. 3 was designed such that all flow diagnostics were performed ≈ 0.28 m downstream of the splitter plate trailing edge. At this location, 13 Kulite XT-140-10D unsteady pressure transducers were mounted flush and wall-normal to the interior of the test section in a vertical array, with each transducer separated by a distance of $\approx 1.3 \times 10^{-2}$ m. Temperature measurements were taken at the same vertical positions as the pressure transducers, using a Constant Current Anemometer (CCA) or "cold-wire" probe. The cold-wire probe was inserted at the centerline of the test section, displaced ≈ 0.05 m horizontally from the pressure transducer array. In total, 11 cold-wire measurement points were obtained with vertical positions corresponding to pressure transducers 2-12. All flow diagnostic signals were recorded using a National Instruments PXIe-1078 DAQ system

at a sampling rate of $f_s = 30{,}000$ Hz, and synchronized with the harmonic signal driving the voice coil actuators to ensure a 0° phase offset between flow forcing and data acquisition.

A complete description of the governing derivations and thermodynamic modeling of the cold-wire can be found in Ref. 2; however a brief overview is given here. Fundamentally, this technique leverages the predictable, temperature-dependent electrical resistance of a microscopic wire filament to track unsteady thermal fluctuations within a fluid flow. Under the supplied constant current, the voltage across the wire is.[14]

$$V' = I_w \alpha R_{w,0} T'_w, \tag{4}$$

Here, $R_{w,0}$ and T_w are the resistance at some reference state and the fluctuating temperature component of the wire, respectively. The temperature coefficient of resistance is denoted by α and I_w is the constant current supplied to the cold-wire (5 mA in this study). Assuming negligible self heating, the wire temperature fluctuations closely track the fluid temperature fluctuations, $T'_f \approx T'_w$, thus functioning as a thermistor and yielding

$$T'_f \approx \frac{V'}{I_w \alpha R_{w,0}} \qquad T'_f \approx \frac{V'}{S}. \tag{5}$$

Here, the sensitivity coefficient, S, is defined as $S = I_w \alpha R_{w,0}$ which can be determined under quiescent conditions.[14] For this study, S was found using a feedback-controlled plenum in which the temperature was varied at regular intervals from 77.4°F to 180.0°F (≈ 300-355 K) and the voltage across the cold-wire was recorded. The resulting data and linear fit via least-squares regression is shown in Fig. 4.

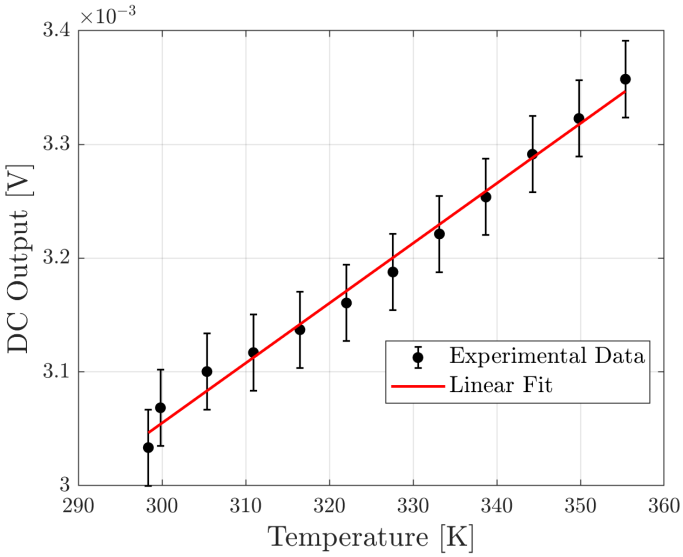

Figure 4: Cold-wire thermal sensitivity calibration data

The error bars constitute the standard uncertainty (68% confidence interval) constructed by combining statistical uncertainty over the sampling period and systematic uncertainty introduced by the instrumentation in quadrature. The resulting sensitivity for the present cold-wire was found to be $S \approx 5.3 \times 10^{-6}$ V/K.

In practice, however, the wire temperature fluctuations, T'_w, do not occur simultaneously with the fluid temperature fluctuations T'_f, as the thermal inertia of the wire causes its response to act as a first order low pass filter.[14] For such a first order system, we can denote the wire thermal time constant as τ_w, with the associated transfer function

$$H(\omega) = \frac{1}{1 + j\omega\tau_w}, \qquad \hat{T}'_w(\omega) = H(\omega)\,\hat{T}'_f(\omega), \tag{6}$$

where the hat denotes Fourier Transformation. By experimentally determining the time constant, τ_w, this transfer function can be used to compensate for the amplitude attenuation and the associated phase lag introduced by

the thermal inertia of the cold wire and to recover the true fluid temperature fluctuations, T'_f. To calculate the transfer function, $H(\omega)$, the step response of the wire was measured using the setup shown in Fig. 5.

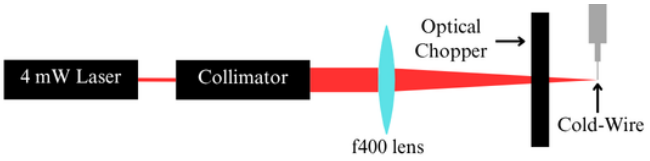

Figure 5: Experimental setup used to determine the time constant of the cold-wire CCA.

A 4 mW laser was brought to a focal point on the cold-wire surface using a beam expander/collimator and an $f = 400$ mm lens. Once aligned, an optical chopper was placed in the focused beam and configured to interrupt the beam in a step-wise manner (light/no light) at the frequency of 100 Hz. By collecting the cold-wire CCA signal with the data acquisition setup described above, a representative step response could be constructed by block- and ensemble averaging the periodic signal, following an approach similar to that of Ref. 15. The averaged signal was then examined to identify the expected log-linear decay region shown in Fig. 6.

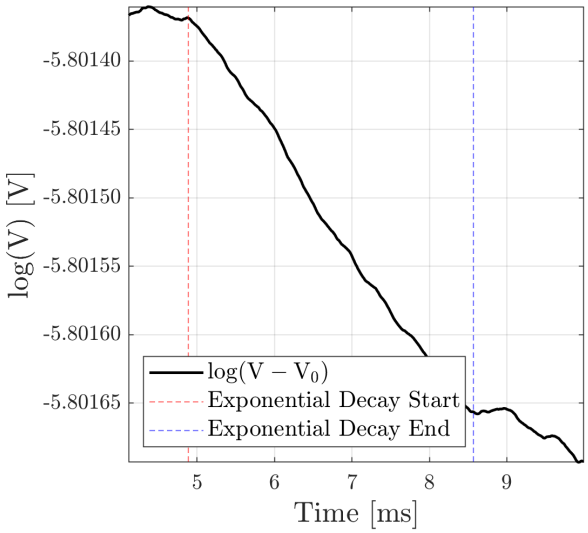

Figure 6: Log-linear decay region used to extract the cold-wire time constant.

The portion of the signal between the annotated start and end of the exponential decay in Fig. 6 was fit to the model

$$V(t) = Ae^{-t/\tau_w} + C \tag{7}$$

using least-squares regression. This procedure yielded a time constant of $\tau_w \approx 1.8$ ms. At the forcing frequency of the shear layer, $f_e = 750$ Hz, the resulting cold-wire transfer function attenuates the signal amplitude by $\approx 88\%$ and introduces a phase lag of $\approx 83°$. Knowing the time constant and using the transfer function in Eq. 6, the measured temperature fluctuations were subsequently corrected for in post processing via forward and inverse Fourier Transforms.

2.3 Optical Techniques

For this study, two optical techniques were employed to estimate the density of the shear layer. The first technique was digital holographic wavefront sensing (DHWFS). DHWFS is an interferometric method that reconstructs aberrated wavefronts by analyzing the spatial frequency of an interference pattern. This pattern is formed on a camera sensor by combining a signal beam and a tilted reference beam in an off-axis, pupil-plane geometry. With

the flow on, density perturbations in the flow alter the local index of refraction according to the Gladstone-Dale equation (Eq. (1)). These refractive changes modify the interference pattern's spatial frequency content, allowing the phase, and ultimately the wavefront, to be recovered via Fourier analysis. The recovered wavefront relates directly to the density and index of refraction along the optical path:

$$W(x,y,z,t) = -\int_0^L n'(x,y,z,t), \mathrm{d}z = -\mathrm{KGD}\int_0^L \rho(x,y,z,t), \mathrm{d}z. \tag{8}$$

Consequently, these wavefront measurements yield a path-integrated approximation of the density field at the measurement location,

$$\rho_L(x,y,t) = -\frac{1}{L}\int_0^L \rho(x,y,z,t), \mathrm{d}z. \tag{9}$$

The severity of aero-optical distortions induced by these density perturbations is typically quantified using the optical path length (OPL),[5]

$$\mathrm{OPL}(x,y,t) = \int n(x,y,z,t), \mathrm{d}z = \int \left[1 + \mathrm{KGD}\rho(x,y,z,t)\right], \mathrm{d}z, \tag{10}$$

or the optical path difference (OPD). The OPD is defined as the deviation of the OPL from its spatially averaged value:

$$\mathrm{OPD}(x,y,t) = \mathrm{OPL}(x,y,t) - \langle \mathrm{OPL}(x,y,t)\rangle = \mathrm{KGD}\int_A^B \rho'(x,y,z,t), \mathrm{d}s. \tag{11}$$

To evaluate the overall intensity of these aberrations and to detect spanwise non-uniformities, it is useful to calculate the time-average of the spatial root-mean-square of the OPD ($\mathrm{OPD}_{\mathrm{RMS}}$):[5]

$$\mathrm{OPD}_{\mathrm{RMS}} = \sqrt{\frac{1}{A}\int_A \overline{\left(\mathrm{OPD}(x,y,t) - \langle \mathrm{OPD}(x,y,t)\rangle(x,y)\right)^2}, \mathrm{d}x, \mathrm{d}y}. \tag{12}$$

For this study, off-axis digital holographic measurements were taken using two different configurations. The first configuration, shown in Fig. 7, provides spanwise, path-integrated density measurements propagated horizontally relative to the laboratory environment.

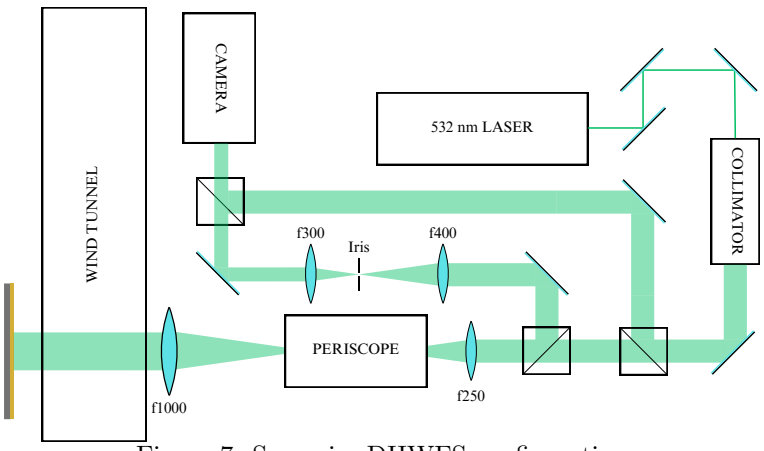

Figure 7: Spanwise DHWFS configuration

In this setup, a 532 nm yttrium aluminum garnet (YAG) continuous-wave solid-state laser is passed through a collimator, expanding the beam to 25.4 mm (1 inch). This expanded beam is then split into reference and signal components. The reference beam is routed directly to the sensor of a Phantom TMX-5010 high-speed camera, recording at $f_s = 30{,}000$ Hz. Meanwhile, the signal beam is further expanded to a diameter of 95.3 mm

(3.75 inches) and centered on the primary streamwise measurement location (depicted in Fig. 3). The signal beam traverses the test section in a double-pass configuration before being reduced to 19.1 mm (0.75 inches) in diameter, ensuring proper overlap with the reference beam on the camera sensor.

The second, cross-stream, configuration is shown in Fig. 8 and utilizes a similar layout as its spanwise counterpart with two major modifications. The first being the test section for spanwise measurements was exchanged for a test section of identical geometry with optical windows oriented vertically instead of horizontally. Second, an additional gold-plated mirror was placed beneath the test section to direct the signal beam upwards through the test section after expansion and propagate the beam vertically relative to the laboratory environment.

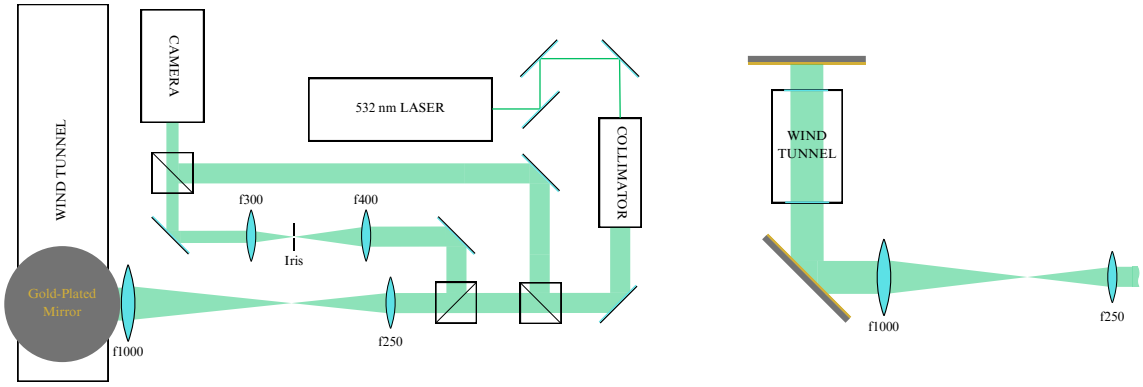

(a) **(b)**

Figure 8: Top view of cross-stream DHWFS configuration (a), side view of cross-stream DHWFS configuration

While useful to examine spanwise uniformity and to identify vortex core locations, the path-integrated nature of DHWFS limits our ability to directly compare against the two-dimensional simulations in Ref. 3. In light of this, a second optical diagnostic technique, self-aligned focused Schlieren (SAFS), was employed in this study to provide density measurements with greater two-dimensionality. The principle of operation for SAFS is the same as the more commonly used focused schlieren with one primary modification: while traditional focused schlieren utilizes a separate source grid and cut-off grid (also known as Ronchi ruling) to act as the light source and knife's edge respectively, self-aligned focused utilizes a series of polarizing optics to allow a single Ronchi ruling to act as both the source and cut-off grids. This modification greatly reduces the sensitivity of the system by removing the need for precise alignment of source and cut-off grids. The SAFS system used in this study is shown schematically in Fig.9. A pulsed high-power LED (Luminous Devices CBT-90-RX-L15-B101) with a wavelength of 621 $\pm$ 6 nm was passed through a two lens system consisting of an f = 16 mm condenser lens and an f = 300 mm plano-convex lens. The LED source and lenses were positioned to image the LED source onto a 4 lp/mm Ronchi-ruling (Applied Image R34-24-CG) which acts as both the source and cutoff grid. Before reaching the Ronchi ruling, the light from the LED is passed through a linear polarizer to create vertically polarized light which is reflected onto the Ronchi ruling with a polarizing beam-splitter. Once passed through the Ronchi ruling, the light forms a striped source pattern which is transmitted through a Ronchon prism without distortion due to the vertical polarization of the light. The vertically polarized, striped source pattern is then expanded and imaged onto a retro-reflective background using a field lens whose object and image planes correspond to the Ronchi ruling and retro-reflective background respectively. Similarly, the plane of interest (shear layer) and the camera sensor plane are their own object-image plane conjugate pair for the given field lens. After passing through the shear layer, the light becomes aberrated, changing the optical path of individual rays through Eq. 1. This distorted light is circularly polarized when it encounters the quarter-wave film placed on the surface of the retro-reflective background, and then horizontally polarized on its second pass through the quarter wave film after reflection. Because the light is now horizontally polarized, the Rochon prism will now slightly deflect the returning beam. This slight deflection causes an offset of the beam relative to the Ronchi ruling, positioning the focused light from the conjugate object plane at the retro-reflective background at the edges on the Ronchi ruling, effectively

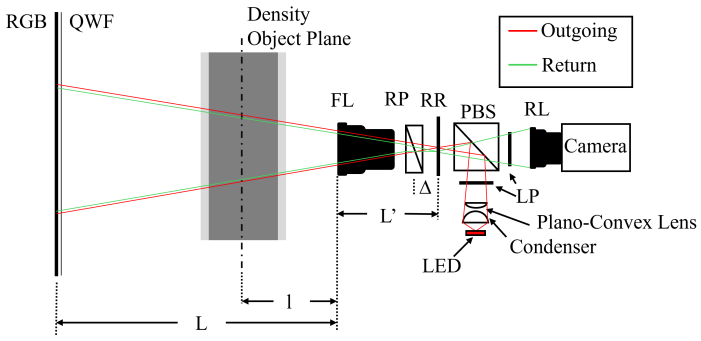

Figure 9: Self-Aligned Focusing Schlieren setup

creating an array of knife edges which operate under the same principles as focused schlieren. As such, density perturbations (and therefore index-of-refraction variations) within the shear layer will slightly change the angles of rays passing through the density object plane, created bright and dark regions corresponding to positive and negative density gradients. After this, the conjugate image plane is recorded in focus on the camera sensor once passing through the polarizing beam splitter and horizontally oriented linear polarizer. A full list of the utilized equipment and relevant specifications are included in Table 1.

Table 1: Self-aligned focusing schlieren components.

Component	**Supplier**	**Model Number**	**Specifications**
Camera	Phantom	KT1210	12,000 fps @ 1280×860
Light Source	Luminous Devices	CBT-90-RX-L15-B101	621 ± 6 nm
Field Lens	Nikon	AF-S NIKKOR	$f = 300$ mm, $f/\# = 4$
Relay Lens	Sigma	EX DG Macro	$f = 105$ mm, $f/\# = 2.8$
Linear Polarizer	Edmund Optics	#66-183	∅50.8 mm
Ronchi Ruling	Applied Image	R34-24-CG	4 lp/mm
Rochon Prism	United Crystals	–	Glass/Quartz, 50×50 mm, 0.125°
Retro-reflective Background	3M	7610	–
Quarter Wave Film	Edmund Optics	#14-725	–
Polarizing Beam Splitter	Thorlabs	PBS519	50.8 mm

The strength of this technique is that the depth of field of the image recorded by the sensor plane is dictated by the field lens used in the system, and as such, may be reduced until the recorded volume is sufficiently two-dimensional. However, the influence of the field lens introduces a principal limitation of the technique: the depth of field and field of view are positively correlated under this configuration. That is, a larger field of view corresponds to a larger depth of field, and therefore greater path integration through the measurement volume. As such, to minimize the depth of field of the system, it is necessary to also minimize the field of view. Under the current geometry, this field of view corresponding to the minimal depth of field was less than the vorticity thickness of the shear layer and was unable to capture full shear layer structures as they convect through the measurement volume. Instead, the field of view was increased to capture two vorticity thickness lengths in the x and y directions at the cost of depth of field and density gradient sensitivity.

Results

All results presented in this section are computed on a phase-averaged basis. A complete period is defined by the ratio f_s/f_e, yielding 40 frames per period based on a sampling rate of $f_s = 30,000$ Hz and a fundamental excitation frequency of $f_e = 750$ Hz. Physical coordinates are normalized by the local vorticity thickness,

$$\delta_w = \frac{U_2 - U_1}{\left(\frac{\partial U}{\partial y}\right)_{\max}}, \tag{13}$$

using velocity components derived from the profile reported in Ref. 8, which established $\delta_w \approx 0.0308$ m. For the non-optical flow diagnostics (pressure and temperature), the shear layer centerline ($y/\delta_w = 0$) is defined as the vertical position where the maximum pressure fluctuation amplitude occurs. Analogously, the centerline for optical diagnostics is identified by the vertical position of the maximum peak-to-peak density fluctuations.

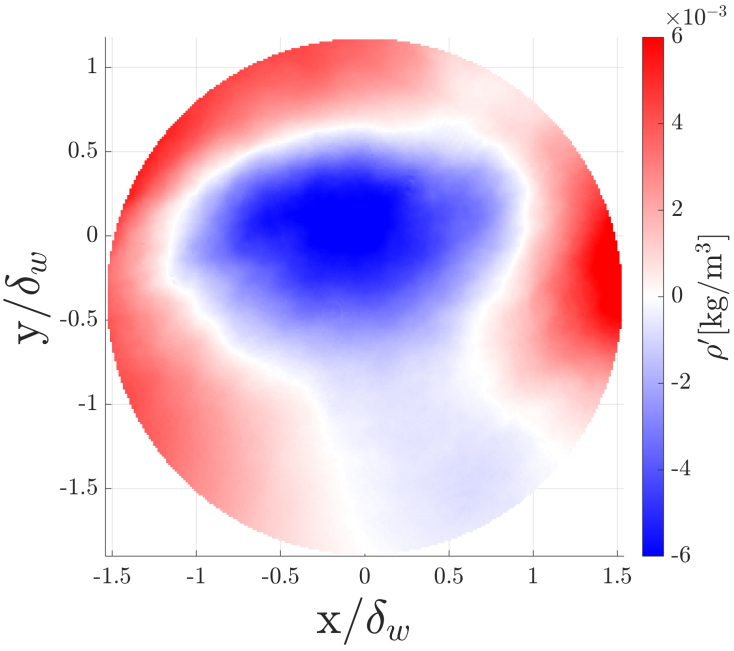

Figure 10: Phase-averaged density field at $\phi = \pi/2$ computed from DHWFS wavefronts

Figure 10 illustrates the phase-averaged spanwise-oriented DHWFS wavefronts, converted into density by manipulating Eq. 8 to yield Eq. 14:

$$\rho'(x, y) = \frac{W(x, y)}{2 \cdot \mathrm{K_{GD}} \cdot \mathrm{L}} \tag{14}$$

The factor of 1/2 in Eq. 14 accounts for the double-pass configuration used during wavefront sensing. To establish an intuitive physical interpretation of these phase-averaged results, it is necessary to first understand the underlying flow structure, specifically, the vortical structures that are responsible for the thermo-fluid mechanisms that drive the optical effects within a subsonic compressible shear layer. Following Ref. 3, a vortex is characterized as a low-pressure, low-density core that entrains surrounding fluid through vortical motion. In phase space, this structure corresponds to a phase offset of $\pi/2$, as shown in Fig. 10. Consequently, the phase offset $\phi_{\mathrm{vortex}} = \pi/2$ will denote the vortex core within the periodic shear layer in the subsequent discussion. For comparison, Fig. 11 presents the two-dimensional density field predicted by the CFD results from Ref. 3, which were computed for flow conditions similar to those in the CSLWT.

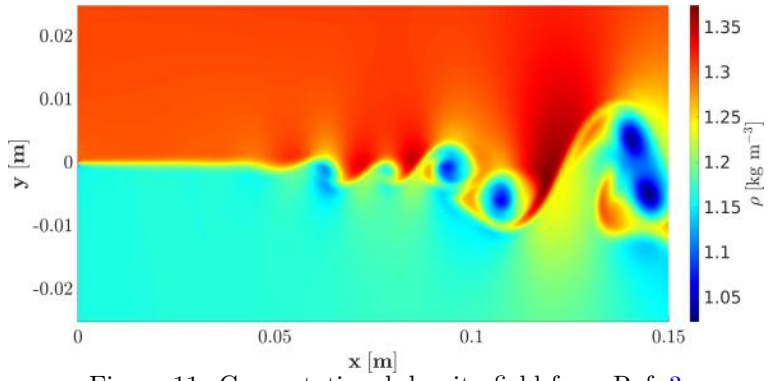

Figure 11: Computational density field from Ref. 3

A prominent distinction between the predicted density field (Fig. 11) and the measured field (Fig. 10) is the magnitude of the density fluctuations. Specifically, the CFD model predicts density fluctuations an order of magnitude higher than those observed experimentally. One possible explanation for this discrepancy is the presence of spanwise non-uniformities along the beam propagation path, such that strong 2-D density variations become attenuated by integration along the beam path. To evaluate this hypothesis, we examine the phase-averaged DHWFS results in the cross-stream configuration.

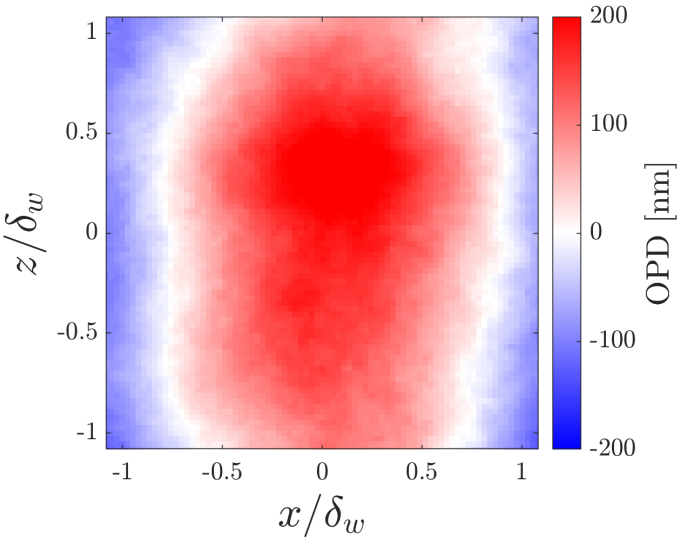

Figure 12: Phase-averaged cross-stream digital holographic wavefront

Upon initial inspection, the phase-averaged wavefront in Fig. 12 appears relatively uniform in the spanwise direction, organizing vortex tubes into periodic vertical streaks. However, spanwise non-uniformities become apparent when analyzing the complete phase-averaged array using the anisotropy ratio, defined as:

$$\beta = \frac{\overline{\mathrm{OPD}}_{\mathrm{RMS,Spanwise}}}{\overline{\mathrm{OPD}}_{\mathrm{RMS,Streamwise}}}. \tag{15}$$

Here, $\overline{\mathrm{OPD}}_{\mathrm{RMS,Spanwise}}$ and $\overline{\mathrm{OPD}}_{\mathrm{RMS,Streamwise}}$ denote the phase-averaged root-mean-square optical path differences in the spanwise and streamwise directions, respectively. The ratio β quantifies the relative strength of spanwise OPD variations compared to streamwise variations, as depicted in Fig. 13.

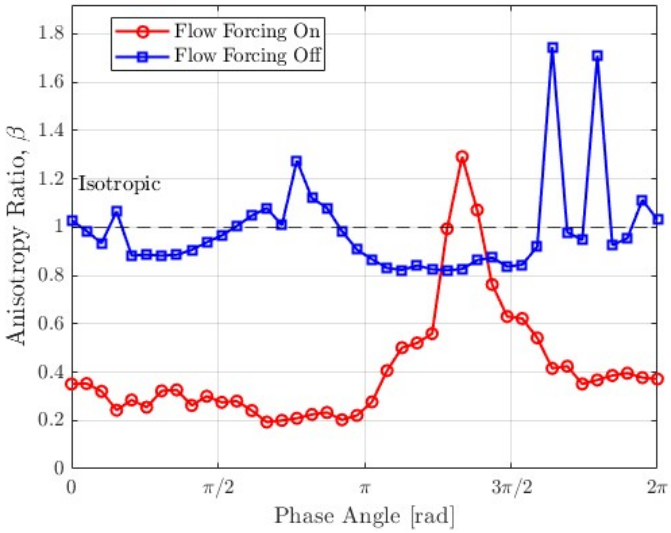

Figure 13: Ratio of $\mathrm{OPD}_{\mathrm{RMS}}$ in spanwise to streamwise directions

A value of $\beta = 1$ indicates isotropic flow with a random distribution of OPD variations. In the unforced case, the natural shear layer is essentially isotropic, experiencing OPD variations of equal strength in all directions. Conversely, the introduction of flow forcing organizes the shear layer into structures with reduced spanwise OPD variations, as intended. Specifically, the $\mathrm{OPD}_{\mathrm{RMS}}$ magnitude decreases by nearly 70% for most of the period, confirming that the applied forcing effectively increases spanwise uniformity. However, the region between π and $3\pi/2$ radians deviates significantly from this trend; here, the flow organizes into a streamwise-oriented structure, indicated by an anisotropy value of $\beta > 1$. The authors suspect this feature is associated with the vortex pairing mechanism, which is driven by the subharmonic forcing frequency (375 Hz) applied at 10% of the fundamental forcing amplitude. This implies that adjacent vortex tubes within the shear layer amalgamate predictably at the measurement location, generating a streamwise-oriented structure that is detectable on a phase-averaged basis.

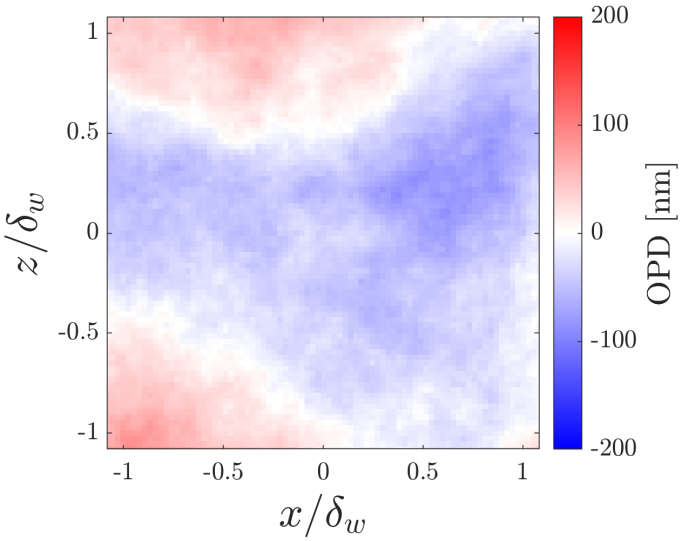

Figure 14: Phase averaged cross-stream digital holographic wavefront for isotropic peak

Figure 14 illustrates the structure associated with this isotropic peak, which shows preferential alignment

with the streamwise direction. It is hypothesized that this alignment is consistent with consecutive vortex tubes undergoing a pairing event. Our interpretation is that as these vortex pairs merge, their co-rotating, low-density, and low-pressure cores entrain each other together and when viewed from the vertical cross-stream direction, this merging process appears as a single, streamwise-oriented low-density structure shown in Figure 14. However, further research is needed to confirm this interpretation. In any case, the remaining OPD fluctuations in the spanwise direction with flow forcing are still not negligible and will serve to heavily aberrate a beam integrated through such a flow field twice for a double pass configuration. As such, it is reasonable to conclude that spanwise non-uniformities may be to blame for the order of magnitude disagreement in terms of density fluctuations between Fig. 11 and Fig. 10.

The results shown above highlight the continued need for an experimental method capable of delivering density measurements on a near two-dimensional basis in order to remove the effects of path-integration. To address this, this study utilized SAFS. As previously described, the current configuration must balance the field of view and depth of field in order to capture the extents of the relevant flow structures and while maintaining a high degree of two-dimensionality. Consequently, these counteracting parameters yielded measurements that were insufficient for identifying the density structures of interest in the subsonic shear layer, as illustrated in Fig. 15.

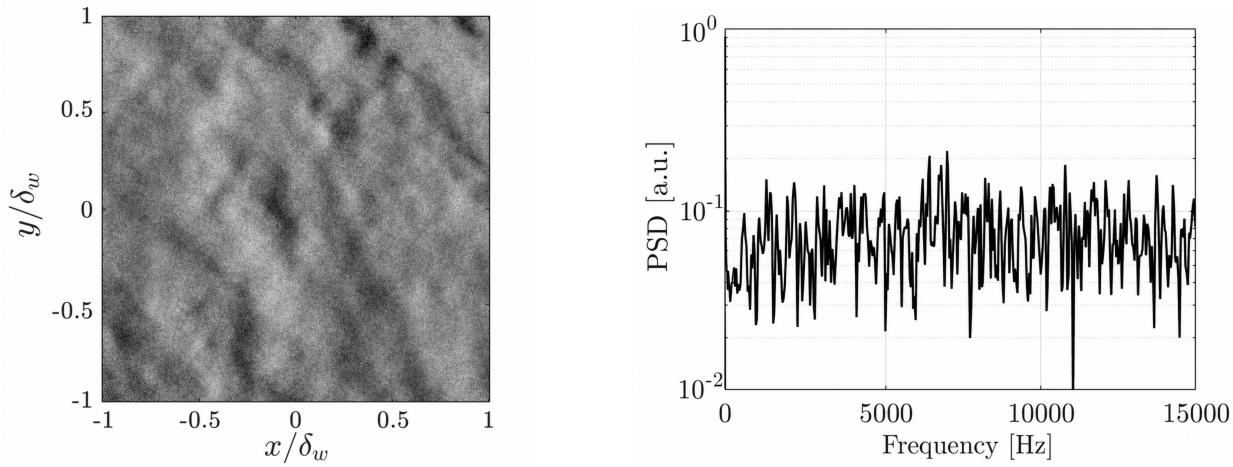

(a) Representative frame (b) Ensemble averaged power spectral density

Figure 15: Self-aligned focusing schlieren (SAFS) measurements.

As we can see from Fig. 15a, with a field of view wide enough to capture one length of vorticity thickness in any direction creates a depth of field which is simultaneously too large to be considered to approximate two-dimensional flow and insufficiently sensitive to meaningfully capture density gradients in a subsonic compressible shear layer. Figure 15b further emphasizes this point by showing the power spectral density (PSD) of the center point shown in Fig. 15a across all frames. If the signal strength within Fig. 15a was sufficiently large to surpass the noise flow, we would expect to see a dominant peak near 750 Hz corresponding to the passing of vortical structures. In contrast, Fig. 15b shows a power spectrum consistent with that of broadband noise indicating that the current configuration of SAFS is insufficient for the present flow regime. Despite its increased two-dimensionality compared to its DHWFS counterpart, these results emphasize the continued need for increasingly sensitive two-dimensional density measurements of a subsonic compressible shear layer.

Transitioning into the pressure and temperature flow results, it is important to note when considering phase averaged results, for flow traversing from left to right relative to the spanwise location shown in Fig. 10, structures that pass first appear on the rightmost edge of results shown in phase space. The consequence of this is that the orientation of structures may initially appear counterintuitive, and it is often more useful to visualize the structures mirrored about the vertical axis to interpret them in a streamwise fashion.

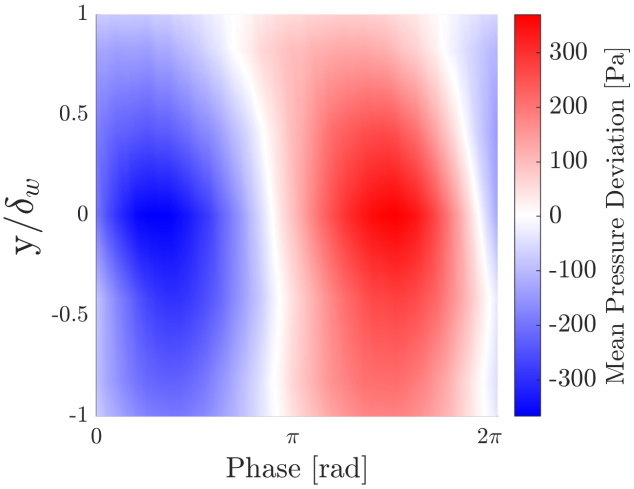

Figure 16: Phase averaged static pressure, P, field.

Beginning with the pressure measurements, the phase location of the static pressure minima in Fig. 16 can be compared to that of the identified low-density vortex core at ϕ_{vortex}. As expected, the two coincide, and the consilience of these flow features confirms the presence of a vortex tube centered on the experimental measurement domain at $\phi_{\text{vortex}} = \pi/2$. From this, the unsteady pressure field, $\partial P/\partial t$, can be computed by taking the temporal derivative of the pressure transducer time series as shown in Fig. 17

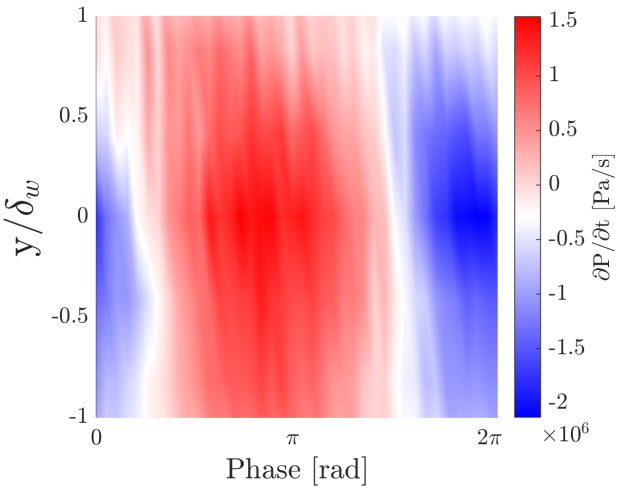

Figure 17: Phase averaged $\partial P/\partial t$ field.

By definition, $\partial P/\partial \phi$ leads the static pressure fluctuations by $\pi/2$. More importantly, at ϕ_{vortex}, a positive $\partial P/\partial t$ well leads the vortex and a negative $\partial P/\partial t$ well trails it, consistent with the rise and fall of the phase-averaged pressure depicted in Fig. 10 and Fig. 16.

The phase-locked static temperature fields, shown in Fig. 18, exhibit the structures expected for the phase-locked vortex at ϕ_{vortex}.

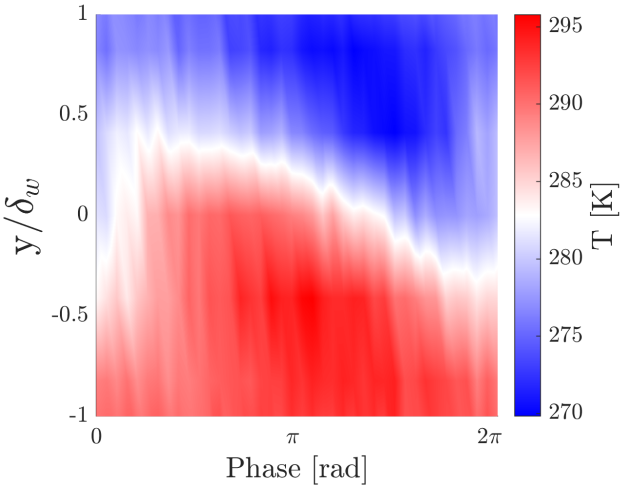

Figure 18: Phase averaged static temperature, T, field.

The temperature difference across the perturbed slip line in Fig. 18 is consistent with the speed differential between the two streams forming the shear layer. The stagnation temperature field in Fig. 19 reveals two vertically offset, co-rotating stagnation temperature lobes. Their existence alone is sufficient to demonstrate that the WCM does not capture the relevant thermodynamics of a shear layer in this regime. Furthermore, the presence of high magnitude stagnation temperature gradients between the lobes reinforces this conclusion, since such gradients were argued in Ref. 1 to be physically inadmissible within the WCM framework.

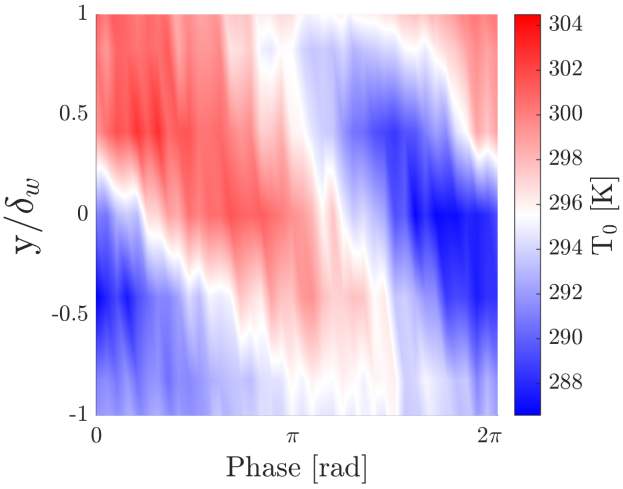

Figure 19: Phase averaged total temperature, T_0, field.

The mechanism producing these stagnation temperature lobes, as proposed in Ref. 3, results from the combined action of vortical motion at the vortex location, ϕ_{vortex}, and the relative positioning of regions with positive and negative $\partial P/\partial t$. Specifically, according to Eq. 2, unsteady pressure-related work performed on fluid particles as they traverse regions of positive $\partial P/\partial t$ increases their total energy (T_0). These particles with higher T_0 continue to rotate around the vortex, producing the high- and low-T_0 "lobes" observed in Fig. 19.

Consequently, the temporal history of particles traversing the pressure wells is essential to the formation of the predicted density gradients in the subsonic compressible shear layer. Because particle paths are driven by the shear layer's vortical motion, adjacent particles frequently traverse $\partial P/\partial t$ wells of opposite signs, resulting

in neighboring particles developing total temperatures with large difference. This process generates steep total temperature gradients, and subsequent density gradients, driven primarily by the temporal history of the thermodynamic fields. Because this temporal mechanism is omitted by the WCM, the observed positioning of co-rotating total temperature lobes and unsteady pressure wells with a phase lag of approximately $\pi/2$ radians provides strong experimental support for the thermo-fluid mechanisms proposed in Ref. 3.

CONCLUSION

This study presented simultaneous, phase-averaged experimental measurements of static pressure, static and stagnation temperature, and inferred density fields from DHWFS and SAFS measurements of a forced subsonic compressible shear layer. The shear layer was formed with a convective Mach number of $M_c \approx 0.23$ and regularized using an array of voice-coil actuators driven at its most-unstable and subharmonic frequencies. Static pressure was measured directly with a wall-normal array of unsteady pressure sensors. Static temperature fields were obtained from calibrated cold-wire Constant Current Anemometry corrected for effects of thermal inertia of the wire using a first order model. The cold-wire thermal sensitivity was determined by applying a least squares linear fit to cold-wire data collected at a range of temperatures in a feed-back temperature controlled plenum. The first order transfer function for the cold-wire was constructed via a focused collimated beam and an optical chopper, enabling construction of an average thermal step response to be fit to an exponential model using least squares regression and recover the associated time constant. Off-axis digital holographic wavefront measurements provided estimates of the spanwise and cross-stream averaged density field, to supply a phase reference to identify the shear layer vortical structure and identify the degree of spanwise uniformity. Self-aligned focused schlieren measurements were also conducted to provide an estimate of the two-dimensional density field at the shear layer centerline. However, the positive correlation between depth of field and field of view introduced a principle limitation which made measurements capable of capturing complete flow structures while maintaining two-dimensional signal strength above the noise floor unfeasible.

Three main observations were made from this experimental study, highlighting a critical interplay between localized two-dimensional fluid physics and three-dimensional optical integration. First, the static pressure minima, associated with a pressure well inside the vortical structure, coincide in phase with the low-density vortex cores identified from the wavefront-derived density field, while the unsteady pressure term, $\partial P/\partial t$, exhibits a leading positive region and a trailing negative region aligned with the vortex. Second, complementary cross-stream DHWFS and narrow depth-of-field SAFS measurements suggest that the discrepancy between the density gradients presented in Ref. 3 and this body of work is driven by spanwise non-uniformities which inherently smooth out the intense, localized density gradients across the line-of-sight integration path. Third, the frequency-compensated temperature measurements successfully resolved the stagnation temperature field, revealing two vertically offset, co-rotating lobes separated by sharp gradients that lag approximately $\pi/2$ radians behind the maxima of the unsteady pressure wells.

Taken together, these results constitute experimental evidence that the Weakly Compressible Model (WCM) is fundamentally insufficient to describe the true thermodynamic behavior of a shear layer in this regime. The WCM fails to predict both the sharp stagnation temperature gradients and the offset, co-rotating lobe structure captured in these experiments. Instead, the physical measurements support the thermo-fluidic mechanism proposed in recent numerical simulations presented in Ref. 3,9. Crucially, these findings reconcile a long-standing aero-optical paradox by demonstrating that the WCM's historic success in predicting path-integrated wavefront errors is potentially a consequence of its 2D framework inadvertently mimicking 3D line-of-sight spatial smoothing, rather than accurately capturing the underlying fluid physics.

Future work will utilize advanced optical flow diagnostics with improved spanwise resolution, such as a specialized Focusing Schlieren approach, to isolate discrete two-dimensional planes of the density field and allow for two-dimensional comparisons with complementary numerical simulations. Concurrently, an analog hardware circuit is under development to provide direct, real-time frequency compensation of the CCA performance, eliminating the need for post-process transfer function fitting. Ultimately, combining these high-resolution experimental efforts with 3D computational modeling will allow researchers to explicitly decouple 2D local gradients from 3D path-integration effects, yielding high-fidelity tools to accurately predict and mitigate the optical degradation of weakly compressible and transonic shear layers.

Acknowledgments

The authors of this paper would like to thank Duncan Windisch for his help over the course of this project.

REFERENCES

[1] Fitzgerald, E. J. and Jumper, E. J., "The optical distortion mechanism in a nearly incompressible free shear layer," *Journal of Fluid Mechanics* **512**, 153–189 (Aug. 2004).

[2] Kipp, C. M., "Experimental studies of the thermodynamic fields of a subsonic compressible shear layer," Submitted to the 14th International Symposium on Turbulence and Shear Flow Phenomena (TSFP14), Heidelberg, Germany, July 28–31, 2026 (July 2026).

[3] DeFoor, T. E., Oliva, A. A., and Rennie, M. R., "Computational Investigation of the Thermo-Fluid Mechanisms for Aero-Optical Distortions in a Subsonic Compressible Shear Layer," in [*AIAA SCITECH 2026 Forum*], American Institute of Aeronautics and Astronautics (Jan. 2026). _eprint: https://arc.aiaa.org/doi/pdf/10.2514/6.2026-1150.

[4] Barrell, H. and Sears, J. E., "The refraction and dispersion of air for the visible spectrum," *Philosophical Transactions of the Royal Society of London. Series A, Mathematical and Physical Sciences* **238**(786), 1–64 (1939).

[5] Gordeyev, S., Jumper, E., and Whiteley, M., [*Aero-Optical Effects: Physics, Analysis and Mitigation*], Wiley Series in Pure and Applied Optics, John Wiley & Sons, 1 ed. (2023).

[6] Rennie, M., Ponder, Z., Gordeyev, S., Nightingale, A., and Jumper, E., "Numerical investigation of two-dimensional compressible shear layer and comparison to weakly compressible model," in [*Directed Energy Professional Society, Beam Control Conference, Monterey, CA, 3-7 March 2008*], (Jan. 2008).

[7] Visbal, M., "Numerical simulation of aero-optical aberration through a weakly compressible shear layer," in [*39th AIAA Fluid Dynamics Conference*], AIAA Paper 2009-4298 (2009).

[8] Kipp, C. M., Bukowski, T., Rennie, R., and Gordeyev, S., "Simultaneous shack-hartmann and digital holography measurements of the optical effect of a subsonic compressible shear layer," in [*Unconventional Imaging, Sensing, and Adaptive Optics 2025*], **13619**, 136190P (2025).

[9] Oliva, A., DeFoor, T., and Rennie, R., "Computational investigation of aero-optical discrepancies in a free shear layer," in [*Unconventional Imaging, Sensing, and Adaptive Optics 2025*], **13619**, 136190N (2025).

[10] Kipp, C., Bukowski, T., Rennie, R., and Gordeyev, S., "Comparison of Shack–Hartmann and digital holographic measurements of the optical effect of a subsonic compressible shear layer," *Optical Engineering* **65** (Apr. 2026).

[11] Papamoschou, D. and Roshko, A., "The compressible turbulent shear layer: an experimental study," *Journal of Fluid Mechanics* **197**, 453–477 (Dec. 1988).

[12] Rennie, M., Duffin, D., and Jumper, E., "Characterization of a Forced Two-Dimensional, Weakly-Compressible Shear Layer.," in [*38th Plasmadynamics and Lasers Conference*], *Fluid Dynamics and Co-located Conferences*, AIAA Paper 2007-4007 (June 2007).

[13] Duffin, D. A., *Feed-Forward Adaptive-Optic Correction of a Weakly-Compressible High-Subsonic Shear Layer*, thesis, University of Notre Dame (Apr. 2009).

[14] Bruun, H. H., [*Hot-Wire Anemometry: Principles and Signal Analysis*], Oxford University Press (May 1995).

[15] Arwatz, G., Bahri, C., Smits, A. J., and Hultmark, M., "Dynamic calibration and modeling of a cold wire for temperature measurement," *Measurement Science and Technology* **24**, 125301 (Oct. 2013).